

The influence of nucleation on cavitation inception in turbulent shear layers

E. S. C. Allan, L. Barbaca, P. S. Russell, J. A. Venning, B. W. Pearce and P. A. Brandner

(Australian Maritime College, University of Tasmania, Australia)

ABSTRACT

The influence of nucleation on cavitation inception in a high Reynolds number turbulent shear layer in the wake of a backward facing step was investigated using a controlled nuclei population. The flow was seeded with near monodisperse nuclei through a single injection port upstream of the step. The spatial distribution of the nuclei concentration within the resulting plume was characterized using a volumetric nuclei measurement technique based on Mie-Scattering Imaging. Incipient cavitation events were captured using two high-speed cameras, mounted to the side and below the tunnel test-section, triggered simultaneously with acoustic measurements. Seeding the flow with large nuclei addressed the issue of secondary re-nucleation in the step re-circulation zone and onset of developed cavitation observed for the flow with the natural nuclei population. Ability to discern individual incipient events enabled examination of the effect of cavitation number and the number of injected nuclei on the inception event rate. The event rate was found to follow a power law with cavitation number and to be linear with the injection rate. The inception events were mainly detected within the boundaries of the nuclei plume, however, a considerable number of out of plume events were observed. This was linked to capture of injected nuclei and/or generated cavitation products in the step re-circulation zone and their dispersion across the tunnel span due to flow three dimensionality. This suggests that the use of a more two-dimensional geometry with limited volume of re-circulation to capture and store nuclei might be beneficial. Notwithstanding these issues, mapping of spatial distribution of cavitation susceptibility, obtained by combining the spatial distribution of cavitation events and nuclei concentration, compare favourably with those reported for the same geometry in the literature. The current work provides a valuable dataset for development of computational tools for modelling of cavitation inception in nucleated flows.

INTRODUCTION

Hydrodynamic cavitation is an undesirable phenomenon detrimental to the performance of naval platforms, in particular their acoustic signature. In order to avoid the occurrence of cavitation, understanding of the underlying flow physics controlling cavitation inception is of paramount importance.

The area of a naval platform particularly susceptible to cavitation is that in the vicinity of the propulsor. The flow around the propulsor is characterized by a series of vortical systems undergoing complex interactions resulting in an unsteady pressure field. Modelling the flow around a propulsor is a challenging and expensive task and to gain fundamental understanding of the physical processes and phenomena involved with vortex interactions it is beneficial to study a canonical flow topology. An example of a suitable flow topology featuring complex vortical interactions is that associated with the turbulent shear layers in the wake of a backward-facing step.

The turbulent flow in the shear layer developing downstream of a backward-facing step (BFS) consists of primary spanwise vortices and weaker vortical braids of quasi-streamwise (QSV) orientation (Bernal & Roshko, 1986; Lasheras *et al.*, 1986). It has been shown, that interactions between these systems can induce large pressure fluctuations where, due to vortex stretching, instantaneous pressure values in the cores of the QSVs can be lower than those in the cores of the nominally stronger spanwise vortices (Katz & O'Hern, 1986; O'Hern, 1990; Iyer & Ceccio, 2002).

The stochastic nature of the unsteady pressure fluctuations makes the accurate characterization of the instantaneous pressure field challenging, but recent advances in experimental measurements (Agarwal *et al.*, 2020, 2021*a,b*) and numerical modelling (Brandao *et al.*, 2020; Brandao & Mahesh, 2022) have contributed to the better understanding of this aspect of the underlying flow physics.

For cavitation inception to occur it is necessary

that water contains sites of weakness, also termed ‘nuclei’, which are typically found in the form of microbubbles. Water contains a natural microbubble (nuclei) population (Khoo *et al.*, 2020), characterized by a stochastic size and spatial distribution. The stochastic character of the natural nuclei population adds to the complexity of cavitation inception characterization.

Within a recent study of cavitation inception in the wake of a BFS for a natural nuclei population performed at the Australian Maritime College (AMC) Cavitation Research Laboratory (CRL), Barbaca *et al.* (2020) reported a further difficulty with inception characterization. They observed that microbubbles generated during collapse and condensation of initial incipient events get captured within the step re-circulation zone, thus altering the local nuclei content. Microbubbles generated by cavitation are often larger than those contained in natural nuclei population (Khoo *et al.*, 2020) and act as preferential sites for re-nucleation, triggering a compounding effect and onset of developed cavitation.

As it can be seen from the preceding discussion, characterization of cavitation in turbulent shear layers is a highly challenging task, which requires evaluation of the interactions between multiple stochastic parameters. To improve the understanding of the effect of a particular parameter on the inception, its stochastic character must be controlled.

The water tunnel at the AMC CRL is designed with a capability to precisely control the water free and dissolved gas content. In order to study nucleation effects on cavitation, all the nuclei are removed from the water, which can then be artificially seeded with a controlled nuclei population. The stochastic character of the tunnel nuclei content can be reduced by seeding the tunnel with a monodisperse microbubble population, i.e. where all the bubbles are of the same size and equally susceptible to cavitation (Franc & Michel, 2004).

Within the scope of current study cavitation inception in the shear layers in the wake of a BFS is characterized for a flow seeded with monodisperse nuclei. Further understanding of the stochastic nature of the nuclei content is gained by seeding the flow through a single injection point (targeted seeding) on the BFS surface and statistically characterizing the resulting nuclei plume using a volumetric Mie-Scattering Imaging (MSI) nuclei measurement technique (Russell *et al.*, 2020*b,a*). High-speed imaging is used to map the probability density function (PDF) of spatial distribution of incipient cavitation events, which, combined with the PDF of spatial distribution of nuclei, is used to obtain a statistical spatial distribution of cavitation susceptibility in the shear layers in the wake of a BFS.

EXPERIMENTAL APPROACH

The experiments were performed in the AMC variable pressure water tunnel. The tunnel test section is 0.6×0.6 m square at the entrance, by 2.6 m long. The test section ceiling is horizontal, with the floor sloping 20 mm over the length to maintain nominally constant speed and zero streamwise pressure gradient. The operating velocity and pressure are controlled independently, with ranges from 2 to 12 m/s and 4 to 400 kPa absolute respectively. The tunnel volume is 365 m^3 and is filled with demineralised water. Optical access is provided through acrylic windows on each side of the test section.

The test section absolute pressure is measured, depending on the value, from high or low range Siemens Sitransp absolute pressure transducers models 7MF4333-1FA02-2AB1 (range 0-130 kPa) and 7MF4333-1GA02-2AB1 (range 0-400 kPa) with estimated precisions of 0.13 and 0.48 kPa respectively. The test section velocity is measured from the calibrated contraction differential pressure. Depending on the value, either a high or low range Siemens Sitransp differential pressure transducers models 7MF4333-1DA02-2AB1-Z (range 0-25 kPa) and 7MF4333-1FA02-2AB1-Z (range 0-160 kPa) are used, with estimated precisions of 0.007 and 0.018 m/s respectively. The dissolved gas content of the water is measured using an Endress+Hauser OxyMax WCOS 41 membrane sensor. Further details on the facility can be found in Brandner *et al.* (2006, 2007).

The experimental setup has been developed to study cavitation inception in the shear layers formed in the wake of a nominally two-dimensional (i.e. spanning the whole test section width) BFS, which is schematically represented in figure 1. The model is machined out of three $1000 \times 600 \times 40$ mm PVC sheets glued together to form a 120 mm thick block. The width of the model, w , is 598 mm, ensuring a 1 mm gap between the model and the test section sides. The height of the model is, $h = 100$ mm, resulting with the expansion ratio $ER = H/(H - h) = 1.2$ and aspect ratio $AR = w/h \approx 6$. The model consists of a 800 mm (L_R) long upstream ramp described by a fifth-order polynomial equation: $\frac{y}{L_R} = 0.75(\frac{x}{L_R})^5 - 1.875(\frac{x}{L_R})^4 + 1.25(\frac{x}{L_R})^3$, ensuring that the first and second derivative at the curve edges are equal to zero to prevent undesirable pressure gradients. Due to mechanical considerations, the upstream end of the ramp is truncated to 520 mm and a 100 mm long stainless steel linear ramp is attached upstream resulting with the ramp height of 1.5 mm at the leading edge. Overall length of the ramp, including the PVC and stainless steel section (L_1) is ≈ 620 mm. Downstream of the ramp is a 200 mm (L_2) long horizontal section. The aft part of the model is equipped with two penetrations. The upstream penetration, located 205 mm upstream of the step is 1.6

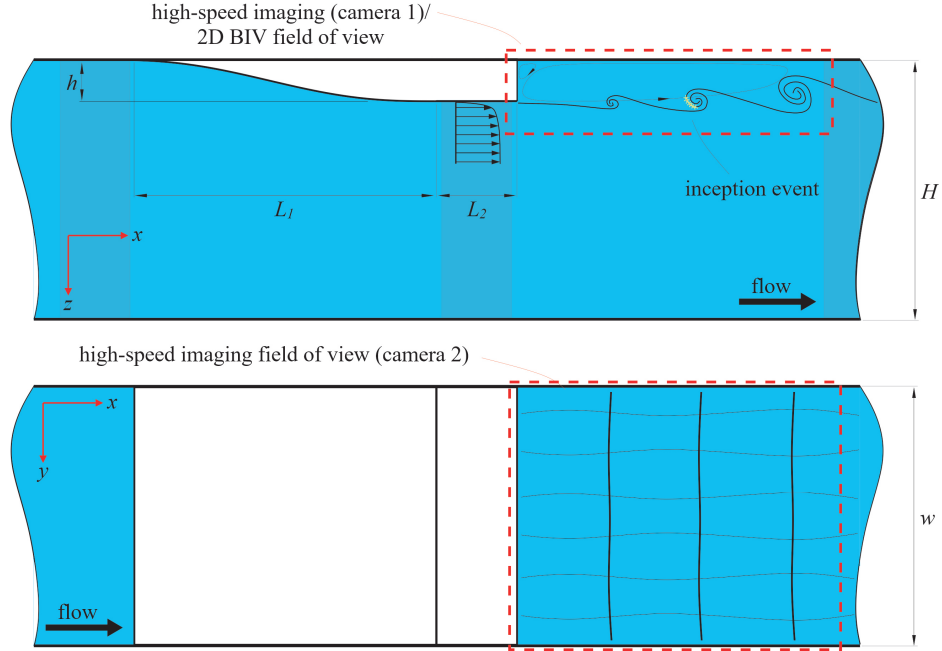


Figure 1: A schematic of the backward facing step model used to study cavitation inception in turbulent shear layers. Side view is shown in the top of the figure and bottom view below. The origin of the coordinate system is located at the step/ceiling junction.

mm in diameter, and is used as the injection port for targeted nuclei seeding. The downstream penetration, located 25 mm upstream of the step is 25 mm in diameter, and is used for boundary layer measurements.

The experiments were performed for a step height based Reynolds number, $Re = Uh/\nu = 1.2 \times 10^6$, where U is the velocity at the streamwise location of the step and ν is the kinematic viscosity of the water. The cavitation number is defined as $\sigma = (p - p_v)/0.5\rho U^2$, where p is the static pressure at the tunnel centreline at the streamwise location of the step, p_v is the vapour pressure and ρ is the water density. Due to the effect of flow contraction induced by the presence of the step, both p and U differ from the tunnel static pressure (p_t) and velocity (U_t) measured at the test section entrance. Therefore, a correction based on the measurement of the pressure coefficient between the test section entrance and the streamwise position of the step (C_p) was applied, giving the equations derived using Bernoulli's principle and based on the measured tunnel parameters, $Re = Re_t/\sqrt{1+C_p}$ for Reynolds number and $\sigma = \sigma_t(1+C_p) + C_p$ for cavitation number. All the measurements were performed for the tunnel dissolved oxygen content between 2.75 and 3.25 ppm.

The boundary layer profile at the nominal position of the step was measured using a 0.7 mm outside, by 0.4 mm inside, diameter total head tube

mounted on a linear traverse. Boundary layer thickness was found to be $\delta = 0.27h$. Further details on the boundary layer measurements and the technique used can be found in Barbaca *et al.* (2020) and Belle *et al.* (2016). Topology of the re-circulation zone downstream of the step was characterized using planar Bubble Image Velocimetry (BIV) measurements and the mean length of the re-circulation zone (\bar{x}_r) was measured as $\bar{x}_r \approx 6h$. Further details on the BIV measurements and the BIV seeding can be found in Barbaca *et al.* (2020) and Barbaca *et al.* (2021)

High-speed imaging of cavitation inception events was acquired using two simultaneously triggered Phantom v2640 cameras mounted to the side and the bottom of the test section. The side camera was equipped with a Nikon AF Nikkor 24 mm f/2.8D lens and the images were acquired at a cropped resolution of 2048×800 pixels giving a field of view of $\approx 930 \times 360$ mm at the tunnel centreline. The bottom camera was equipped with a Nikon AF Nikkor 35 mm f/2D lens at full resolution of 2048×1952 pixels with resulting field of view at the tunnel ceiling covering the full span of the test section and ≈ 780 mm in the streamwise direction. Back-lighting was provided by an Effilux EFFI-BL-LITE-1M12P 650×650 mm LED panel, covering the full area of the test section side window. The image acquisition was controlled via Phantom PCC 3.4.4

software with the external triggering signal provided from a BNC Model 575 delay/pulse generator with a 5 ns accuracy. The images were acquired at 6600 frames per second.

Acoustic measurements were obtained simultaneously with high-speed imaging using a Bruel & Kjaer Type 8103 hydrophone (voltage sensitivity 25.1 $\mu\text{V}/\text{Pa}$). The hydrophone was mounted in a flooded cavity (kept at the same pressure as the tunnel test section) beneath a 10 mm polyurethane diaphragm, with a 149 mm sensing diameter (Doolan *et al.*, 2013). The hydrophone was mounted in the side wall at the test section mid-height, approximately 11h upstream of the step. The signal was conditioned with a Bruel & Kjaer Nexus conditioner and amplifier, which was also used to apply a 0.1 Hz - 100 kHz bandpass filter. The filtered signal was acquired using a National Instruments PXIe-4497 card at a sampling rate of 204.8 kHz.

NUCLEI INJECTION AND MEASUREMENTS

The equilibrium of a microbubble (nuclei) becomes unstable if the flow local pressure is reduced below a critical value, p_c . If the local pressure value remains below p_c for a sufficient time period, the nuclei becomes activated (undergoes explosive growth) and is classified as a site of a cavitation inception event. Nuclei critical pressure is dependent on the nuclei initial size (d_0) and ambient pressure (p_∞) as per equation 1

$$p_c = p_v - \sqrt{\frac{4}{27 \left[\left(\frac{d_0}{4S} \right)^3 (p_\infty - p_v) + \left(\frac{d_0}{4S} \right)^2 \right]}}, \quad (1)$$

where p_v is the water vapour pressure and S is the surface tension. This equation can be derived from consideration of the equilibrium of bubble internal and external pressures and the surface tension assuming isothermal internal gas behaviour and no mass transfer via phase change or diffusion (Franc & Michel, 2004).

The natural nuclei population in the AMC water tunnel has been previously characterized using a Cavitation Susceptibility Meter (CSM) measurements (Venning *et al.*, 2018; Khoo *et al.*, 2020). Measured cumulative size distribution was found to follow a power law like decrease in nuclei concentration with increase in nuclei size, with the largest measured nuclei of the order of 10 μm in diameter. From equation 1, it can be calculated that for the largest nuclei contained within the natural population, the critical pressure is ≈ 5.5 kPa below p_v , or ≈ 2.5 kPa below zero, i.e. for the natural nuclei to get activated the water must be in tension. As the natural nuclei follow a power law the largest nuclei are however present in extremely small concentrations.

As previously discussed, the stochastic nature

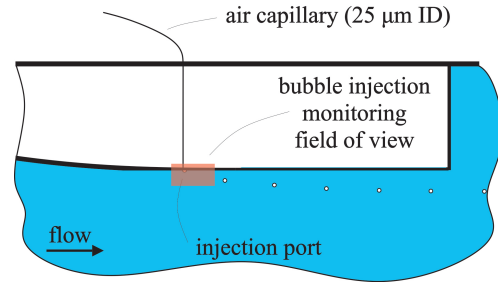


Figure 2: A schematic of the nuclei injection system consisting of a 25 μm diameter air capillary connected to the injection port flush to the BFS surface. Bubbles are produced via inertial pinch-off of the air volume at the injection port outlet due to the high velocity gradient and shear between the injector and freestream flows.

of the water nuclei content can be reduced by artificially seeding the water with a monodisperse nuclei population, where the critical pressure is equal for all nuclei. To ensure that the seeded population is the only active population at a particular cavitation number, p_c for seeded nuclei has to be markedly higher than that for the largest nuclei contained in sufficient concentration within the natural population. To satisfy such requirement, a capability to seed the flow with monodisperse nuclei ≈ 60 μm in diameter ($p_c \approx p_v$) has been developed at the AMC.

Targeted seeding of a high Re flow with a monodisperse population of large nuclei was difficult to achieve. An in-wall nuclei injection system based on the use of a microfluidic T-junction, routinely utilized for the experiments at CRL (Russell *et al.*, 2020b), suffered with issues related to bubble break-up. High velocity gradients and shear between the flow delivering the nuclei through the injector port and the freestream flow induced bubble break-up, with products being generated across a wide range of sizes. Given the stochastic size distribution and uncertainty in the total number of bubbles generated by the bubble break-up process the modified population was deemed neither rigorous nor feasible for use in the current experiment. An injection system with the outlet of the injector tube orientated in the streamwise direction to limit the velocity gradients was trialled, however this also did not yield a satisfactory result.

Following from these observations, a different approach, based on the use of the high wall shear at the injection port as a mechanism for bubble generation, was employed. For this purpose, a novel system incorporating an air capillary with the outlet mounted flush to the injection port at the BFS wall has been developed.

A schematic of the system is presented in figure 2. Pressurized air is delivered to the injection port via

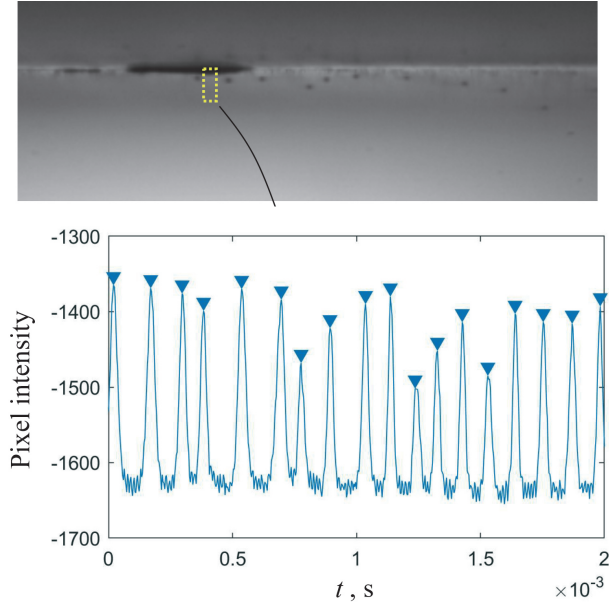


Figure 3: A sample shadowgraph image of the bubble train at the outlet of a capillary tube mounted flush to the backward facing step wall. Bubbles are produced by fragmentation of the air volume by the high shear within the step wall boundary layer. A 3×11 pixels subsample, marked with a yellow box, is used for the analysis of the bubble production rate. A 0.002 s time series of the inverted sum of the pixel intensity of the subsample is shown below the image, with the marked peaks denoting the passage of a bubble.

a 358 mm long $25 \mu\text{m}$ diameter capillary tube, with the supply pressure regulated using a Proportion-Air QPVT1BNSZP10BRGAXL electronic regulator (range 0 - 10 bar) equipped with a Prevost $1 \mu\text{m}$ air filter. The growing air volume undergoes coherent pinch-off similar to T-junction microbubble production through a balance of increasing bubble drag, with increasing wall shear overcoming bubble surface tension.

To examine and monitor the bubble generation process at the injection port, high-speed shadowgraphy imaging of the injector port region (indicated with a red box in figure 2) was performed. The imaging setup utilized for this purpose consists of a Photron Fastcam SA5 high-speed camera with a maximum resolution of 1024×1024 pixels equipped with a Nikon AF-D 200mm f/4 Macro lens. The images were acquired at a reduced camera resolution of 256×64 pixels at 300000 frames per second, with illumination provided from a single Scitech Constellation 120 continuous LED lamp. The generation process was examined for a wide range of combinations of tunnel and air capillary pressures, with the pressure ranges from 75 to 175 kPa and 150 to 450

kPa respectively.

A sample shadowgraphy image of a representative bubble train is shown in figure 3. For each combination of pressures, the train consisted of bubbles ranging between 50 to $70 \mu\text{m}$ in diameter, with the production rate controlled by the differential pressure between the capillary inlet and the tunnel. From equation 1, it can be calculated that the variation in critical pressure between size range extremes of the generated population is about 0.2 kPa and, therefore, the population can be considered as near monodisperse. As the critical pressure at the lower end of the generated population size range is still well above the critical pressure of the largest nuclei contained in sufficient concentration within the natural populations, injected nuclei are sufficiently more susceptible to cavitation inception than the natural nuclei. Based on these two considerations, the population generated via shearing within the BFS wall boundary layer is deemed satisfactory for use in the experiment.

A 3×11 pixel subsample of the image positioned just downstream of the air capillary outlet, noted with a yellow box in figure 3, was used for the analysis of the bubble production rate. A time series of the inverted value of the sum of the pixel intensity across the subsample is shown at the bottom of figure 3. Each time series was analysed using a peak finding algorithm, with the passage of each bubble (shadow in the image) marked with a peak in the inverted intensity.

The bubble production rate dependence on the differential pressure between the capillary inlet and the tunnel was analysed for a tunnel pressure $p = 80 \text{ kPa}$ and capillary pressure range $150 \leq p_{air} \leq 450 \text{ kPa}$, varied in 50 kPa increments. A sample containing 50000 frames was acquired for each condition. Dependence of the bubble production rate, f_b , on the pressure differential between the air capillary inlet and the tunnel, $\Delta p = p_{air} - p$, is presented in figure 4. The injection system is capable of producing bubbles at a rate of the order of 10 kHz , f_b increasing linearly with an increase in Δp at a rate of about 57 Hz/kPa . A linear fit function through the data points is represented with a dashed line in figure 4. For the purposes of the current study, an operating point with $f_b \approx 11 \text{ kHz}$ is selected.

The time series of the subsample pixel intensity indicates that the bubble production rate is not perfectly consistent across the acquired sample, with instantaneous variations in bubble production of about $\pm 200 \text{ Hz}$. However, the time scale of the variations are much shorter than the acquisition periods of nuclei and cavitation inception measurements, and consequently these are unaffected by this small variation of the bubble production rate.

A more detailed description of the presented bubble generation method, including theoretical

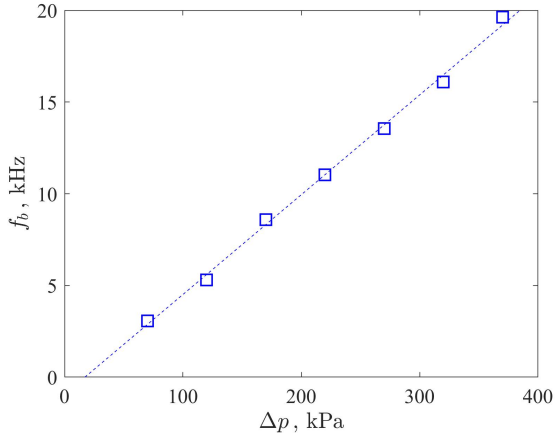


Figure 4: Dependence of bubble production rate (f_b) on the differential pressure between the air capillary inlet and the tunnel (Δp), with $p = 80$ kPa. Linear fit through the data points is denoted with a dashed line.

foundations and a systematic study of the effect of variation in the capillary geometry and flow parameters will be a topic of a separate study to be reported in the near future.

While seeding the flow with near monodisperse nuclei addresses one aspect of the stochastic nature of nuclei content, the spatial distribution of nuclei within the flow still remains a stochastic variable. In order to statistically characterize the spatial distribution of the injected nuclei plume, a volumetric nuclei measurement technique based on use of Mie-Scattering Imaging has been developed.

A schematic representation of the experimental setup used for spatial characterization of the nuclei plume is shown in figure 5. The MSI measurements were acquired using a 48MP IO Industries Flare 48M30 CX high-speed CMOS camera equipped with a Nikon AF-S Nikkor 85 mm f/1.4 lens, located to the side of the test section. Bubbles were illuminated using an Ekspla NL204-SH TEM₀₀ laser emitting 532 nm light with pulse frequency of up to 1 kHz and energy of 2 mJ per pulse. The laser was mounted horizontally below the tunnel test section, with the beam directed into the tunnel using two Thorlabs NB 1-K12 1" Nd:YAG mirrors. The beam entered the tunnel test section through a 80 mm thick acrylic window. To prevent burning of the acrylic window, the laser had to be operated at the lower power output, limiting the lower bound of detectable bubble size range. The beam was angled 7° from the vertical axis to prevent any reflected and refracted rays from overlapping the measurement beam. Accordingly, the camera was rotated so that the horizontal axis was parallel to the

direction of the beam propagation. The camera was set with the sensor plane normal perpendicular to the beam so that the measurement angle was 90°.

Spatial characterization is achieved by jointly traversing the laser beam and the camera across the wake of the BFS. Position of the laser beam is adjusted by traversing the location of the two mirrors directing the beam into the tunnel. Streamwise positioning is achieved by mounting both mirrors on an Isel linear traverse with a 600 mm travel. Mechanical considerations limit measurements to the range of positions from the step up to 500 mm downstream. Spanwise positioning is achieved by mounting the mirror M2 on a Zaber linear traverse with a 200 mm travel attached to the streamwise traverse, enabling measurements 100 mm each side of the tunnel centreline. To maintain the camera streamwise position coincident with the position of the laser beam, as well as the camera defocussed distance, the camera was mounted to an identical traverse setup as the mirrors directing the beam.

Measurements of the nuclei spatial distribution were performed for three streamwise ($x - z$) and five spanwise ($y - z$) planes. Streamwise planes included the tunnel centre plane ($y = 0$) and planes located at $y = 0.2$ and $0.4h$. The increment between measurement points in the streamwise direction was set to $0.2h$. Spanwise distributions were obtained at the locations $x = 1, 2, 3, 4$ and $5h$ downstream of the step. Increment between measurement points in the spanwise direction was set to $0.2h$. As the laser beam is nominally aligned with the vertical axis, vertical distribution is obtained along a continuous line, i.e. did not require incrementation. Due to symmetry of the bubble plume, only one side of the plume was captured for both the streamwise and spanwise distributions.

The plume was characterized for the same flow Re as cavitation inception, but at a non-cavitating σ value to ensure that bubble population is not modified by cavitation products. For each measurement position images were acquired until a statistically significant number of bubbles was detected (minimum of 500 bubble detections). The required number of images varied depending on the bubble concentration across the plume, and accordingly samples of between 50000 and 200000 images were acquired. Given the sampling rate of 500 Hz, image acquisition for all the planes of interest took ≈ 20 hours. The MSI measurement calibration, data processing and analysis were performed using the method developed by Russell *et al.* (2020b) and, for brevity, the details will not be provided here. A high-speed shadowgraphy dataset of the bubble injection through the injector port was acquired every 10 minutes to monitor the bubble production rate.

Contour plots of bubble concentration, C ,

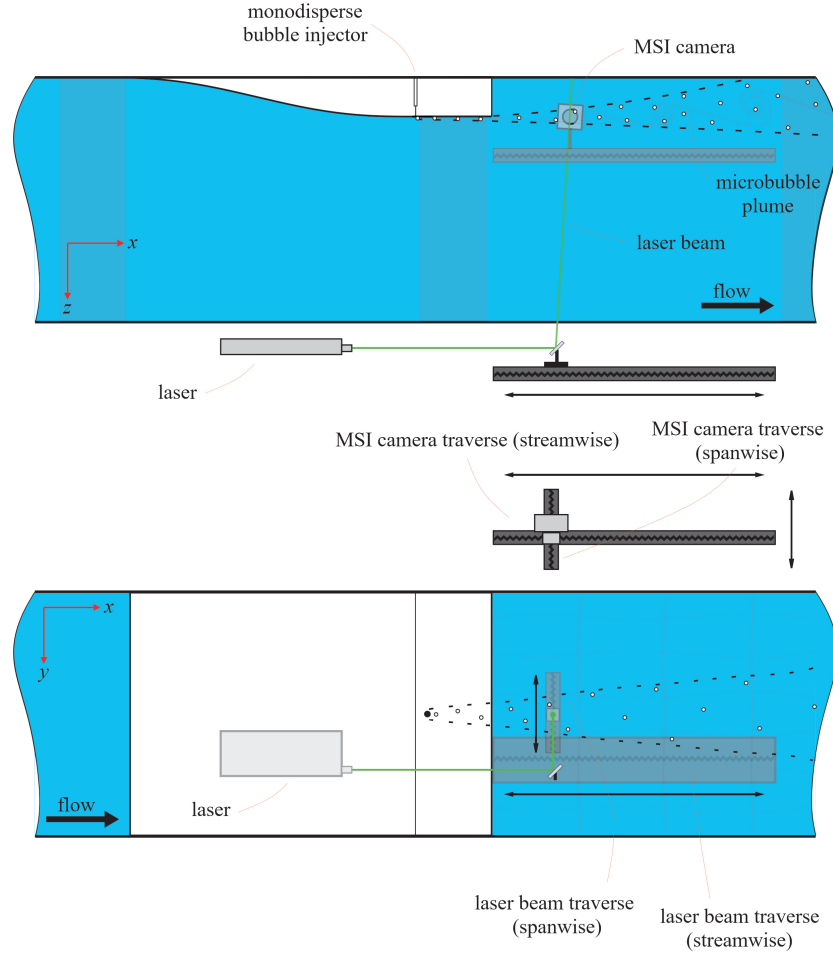


Figure 5: A schematic of the optical system used for the characterization of spatial distribution of nuclei in the wake of the backward facing step. Side view is shown in the top and bottom view in the bottom of the figure. The area shaded with red in side view represents the field of view of shadowgraphy measurements at the location of the nuclei injection port. The traverse system enables MSI measurements of nuclei in the wake of BFS from the step to 5.5 step heights downstream in the streamwise direction and a step height each side of the tunnel centreline in the spanwise direction.

distribution for the streamwise planes are presented in figure 6 and for the spanwise planes in figure 7. Note that due to the wide range of concentration values, color shading is logarithmically distributed. Nuclei are injected at a rate of $f_b = 11$ kHz at a position about 200 mm upstream of the step. The injected plume undergoes limited dispersion within the BFS wall boundary layer as it is advected along the BFS surface. The highest nuclei concentration, $C \approx 1$ mL⁻¹, can be observed for the measurement point closest to the step and located at the tunnel $y = 0h$ plane (injector port plane). As nuclei are advected further downstream of the step, formation and increase in size of the shear layer structures promote dispersion of nuclei in the spanwise directions. This results in an increase in the extent of the nuclei plume

in the $y-z$ plane, and consequent decrease in maximum concentration value in the $y = 0h$ plane. The maximum concentration value decreases about two orders of magnitude between the step and the most downstream measurement location.

The dispersion of the bubbly plume in spanwise directions is also evident in the contour plots of concentration distribution in the $y-z$ planes. It can be seen that for the two most downstream planes ($x = 4$ and $5h$) the plume appears to contract, however, this is the result of very bubble low concentration in this region, which would require an impracticably large dataset to completely resolve.

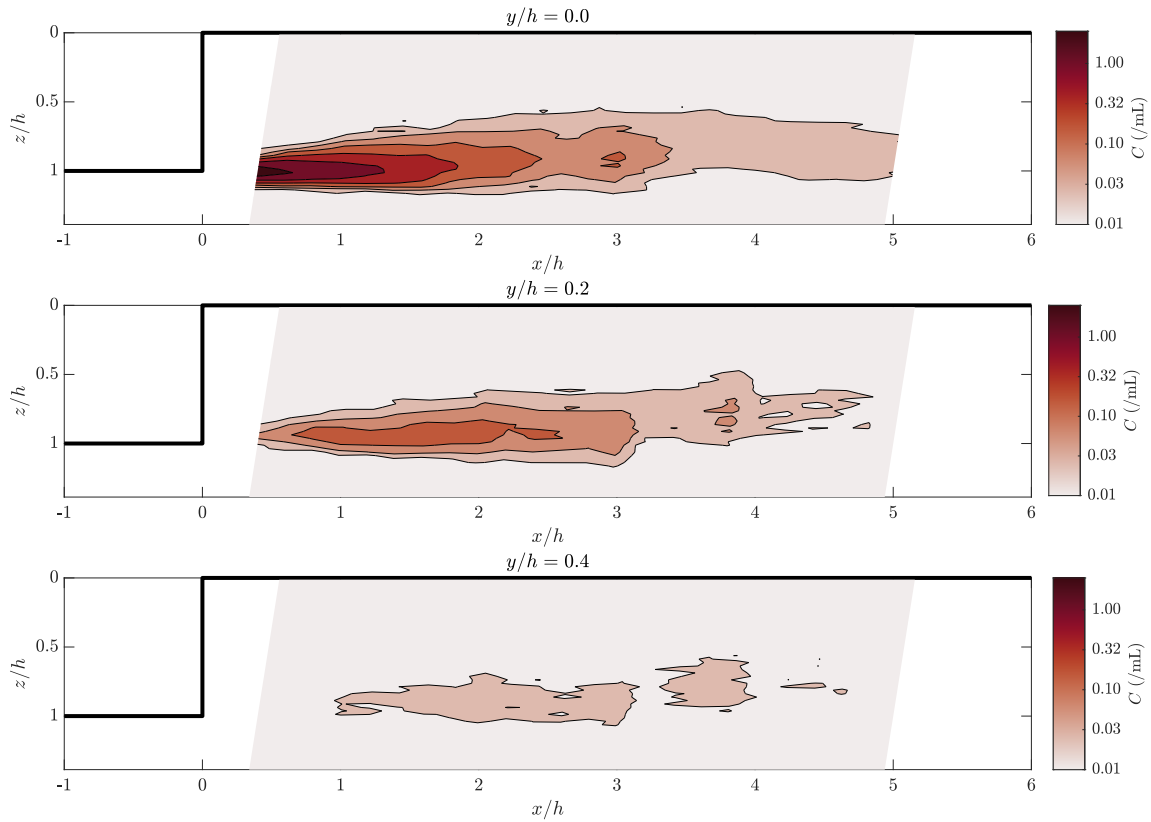


Figure 6: Contour plots of bubble concentration in the wake of a BFS for three streamwise ($x-z$) planes at the spanwise locations $y = 0, 2$ and $4h$, obtained using volumetric nuclei measurement technique based on Mie-Scattering Imaging. Contours indicate the region with highest concentration at the tunnel centre-line just downstream of the step. The bubble concentration reduces with increase in spanwise and streamwise distance from the tunnel centreline and step respectively. Note the logarithmic colorbar and spacing between the contours.

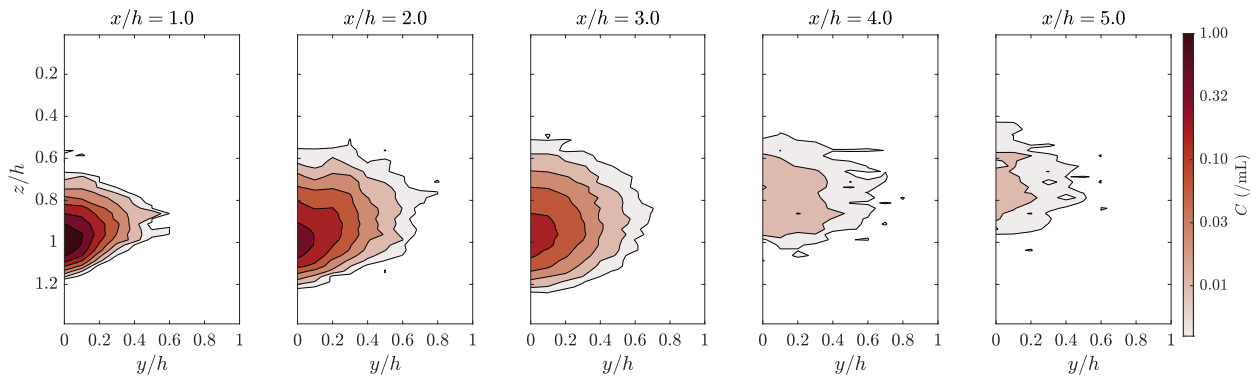


Figure 7: Contour plots of bubble concentration in the wake of a BFS for five spanwise ($y-z$) planes at the streamwise locations $x = 1, 2, 3, 4$ and $5h$ downstream of the step, obtained using volumetric nuclei measurement technique based on Mie-Scattering Imaging. Note the logarithmic colorbar and spacing between the contours.

CAVITATION INCEPTION

Cavitation inception events were observed to occur in the cores of stretched quasi-streamwise vortices contained within the BFS shear layer. Injection of large nuclei resulted with an increase in the value of incipient cavitation number, $\sigma_i \approx 1.2$, in comparison with $\sigma_i \approx 0.65$ reported by Barbaca *et al.* (2020) for the flow with the natural nuclei population. Inception at these higher σ values largely alleviated the issues related to secondary re-nucleation from the cavitation products and immediate formation of developed cavitation at σ_i as observed by Barbaca *et al.* (2020) for the flow with the natural nuclei population. Intermittency of inception enabled discrimination of individual events and assessment of the effect of σ and f_b on cavitation inception rate.

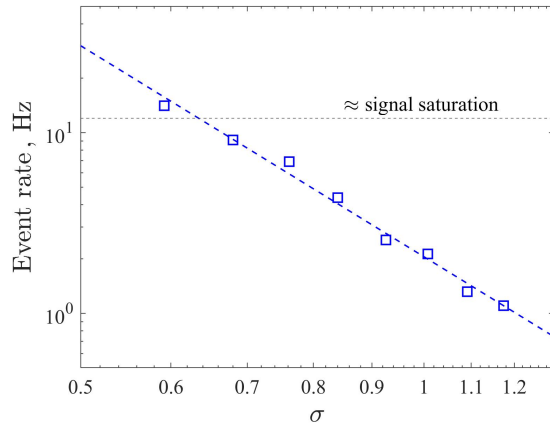


Figure 8: Cavitation inception event rate as a function of cavitation number for a constant bubble injection rate ($f_b \approx 11$ kHz) presented in a $\log - \log$ plot. Event rate increases following a power law with a decrease in σ as marked with a dashed line. The event rates are obtained from the acoustic measurements acquired over a time period of 60 s at a sampling rate of 204.8 kHz. The acoustic signal becomes saturated, i.e. individual events cannot be rigorously discerned, above the event rate of ≈ 12 Hz, as indicated with a dashed horizontal line in the plot.

Dependence of the cavitation inception rate on σ for a constant nuclei injection rate, $f_b \approx 11$ kHz, is presented in figure 8 in a $\log - \log$ plot. The results were obtained from the acoustic measurements acquired over a 60 s period at a sampling rate of 204.8 kHz. In addition to the hardware filtering, a 1 - 10 kHz bandpass filter was applied for processing of the acoustic data. A cavitation event was detected when acoustic pressure exceeds a threshold value set to 25 Pa. To ensure that only individual events are captured, a minimum delay

of 10 ms between the end of an event (acoustic pressure value decreasing below the threshold) and a start of a subsequent event was imposed.

Inception rate increases with a decrease in σ following a power law like behaviour, as marked with a dashed blue line in figure 8. An event rate of ≈ 12 Hz is established as an upper limit for detection of individual events (dashed horizontal line), as for higher values a time overlap between the individual events becomes more prominent. The measured event rate values of the order of 1 to 10 Hz, for the investigated σ range, demonstrate a low probability of a nuclei being captured in a vortex strong enough for activation to occur, with the probability being of the order of 0.01 to 0.1%.

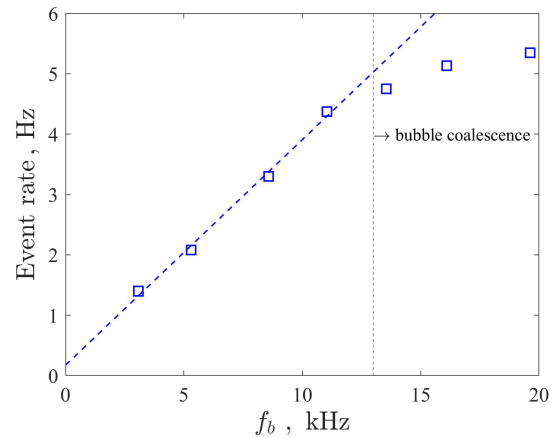


Figure 9: Dependence of cavitation inception event rate on the bubble injection rate for a constant cavitation number, $\sigma \approx 0.85$. Event rate increases linearly (represented with a dashed blue line) with an increase in f_b for $f_b \lesssim 13$ kHz. For the higher f_b values, the rate of increase reduces due to bubble coalescence in the region just downstream of the injection port. The event rates are obtained from the acoustic measurements acquired over a time period of 60 s at a sampling rate of 204.8 kHz.

The gradual increase in the event rate with decreasing σ for the flow seeded with large monodisperse nuclei is in contrast with a step function at $\sigma \approx 0.65$ observed for the natural nuclei population, and is further evidence of the diminished influence of secondary re-nucleation on the cavitation inception in the seeded flow.

The influence of nucleation on cavitation inception was investigated by varying f_b for a constant σ . Cavitation event rate as a function of f_b is presented in figure 9 for $\sigma \approx 0.85$. Event rates are obtained from the acoustic measurements using the same processing as described above. A linear increase in the number of events

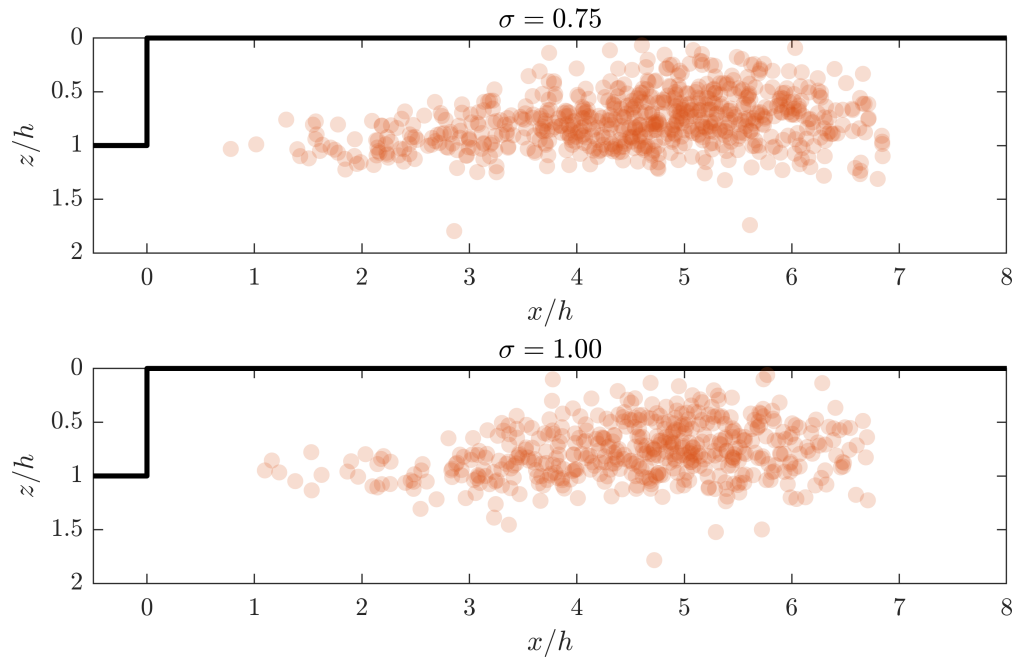


Figure 10: Scatter plots of the locations of all inception events (along the y direction) captured in high-speed videos in $x - z$ plane for $\sigma = 0.75$ and 1. Incipient events start to appear about h downstream of the step and have a peak in the density about $5h$ downstream of the step. Dispersion of the inception locations in z - direction is related to the increase in the size of shear layer structures with increasing distance from the BFS. The BFS is represented with a thick black line in the upper left corner of the plots.

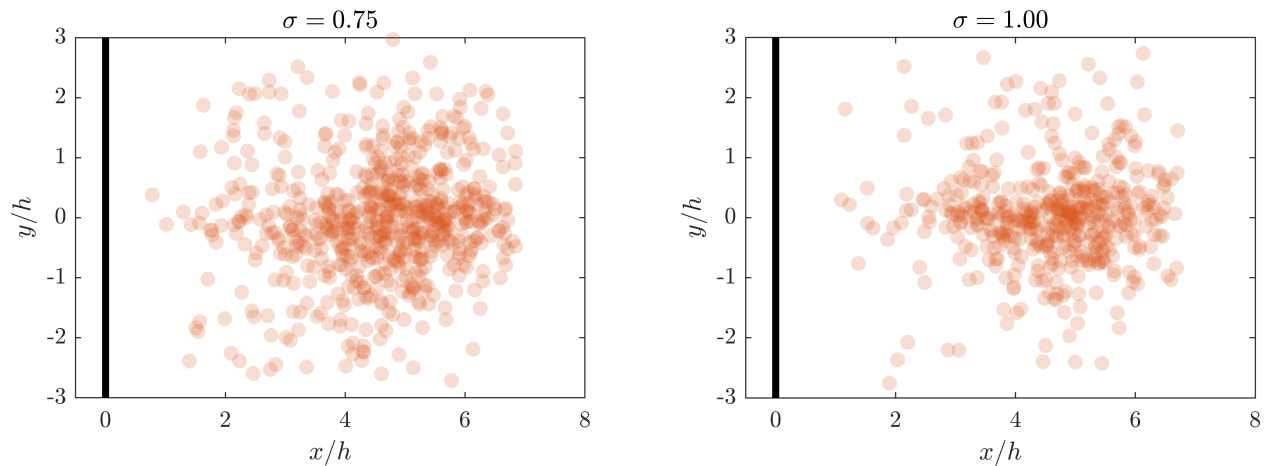


Figure 11: Scatter plots of the locations of all inception events (along the z direction) captured in high-speed videos in $x - y$ plane for $\sigma = 0.75$ and 1. High density of the events is evident within the dispersion boundaries of the plume of injected nuclei. However, a significant number of the events is recorded outside of the injected nuclei plume. The BFS is represented with a thick black line on the left side of the plots.

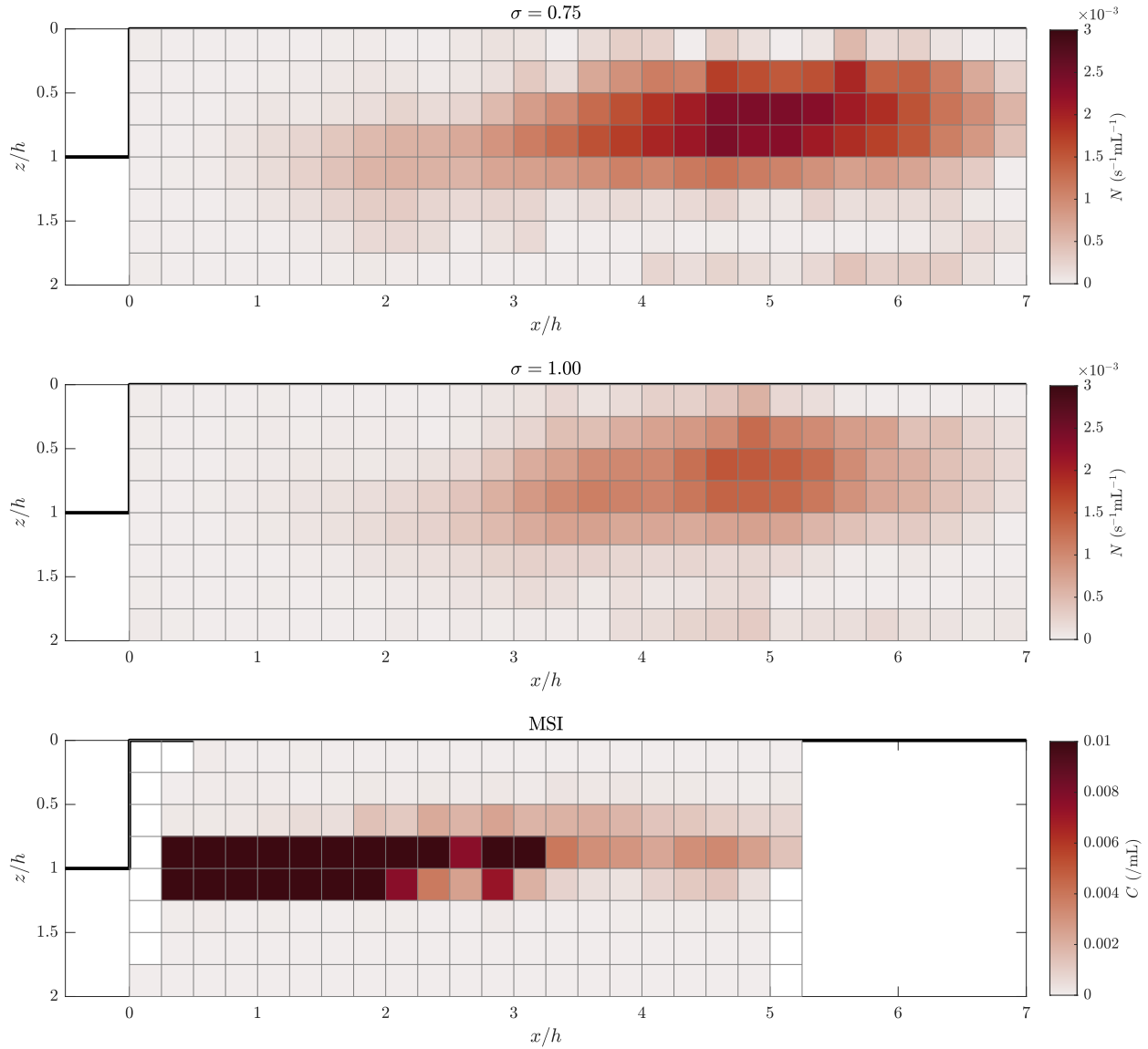


Figure 12: Mapping of the spatial distribution of cavitation inception event rate in the BFS shear layer for $\sigma = 0.75$ and 1. The continuous volumetric data obtained using two high-speed cameras is discretized into cells $0.25 \times 0.25h$ in $x - z$ plane and a $0.25h$ cell at tunnel mid-span in y direction. A second order Savitzky-Golay filter is used to smooth the raw data. Spatial distribution of the nuclei concentration discretized over the same grid is shown in the bottom of the figure. The BFS is represented with a thick black line in the upper left corner of the plots.

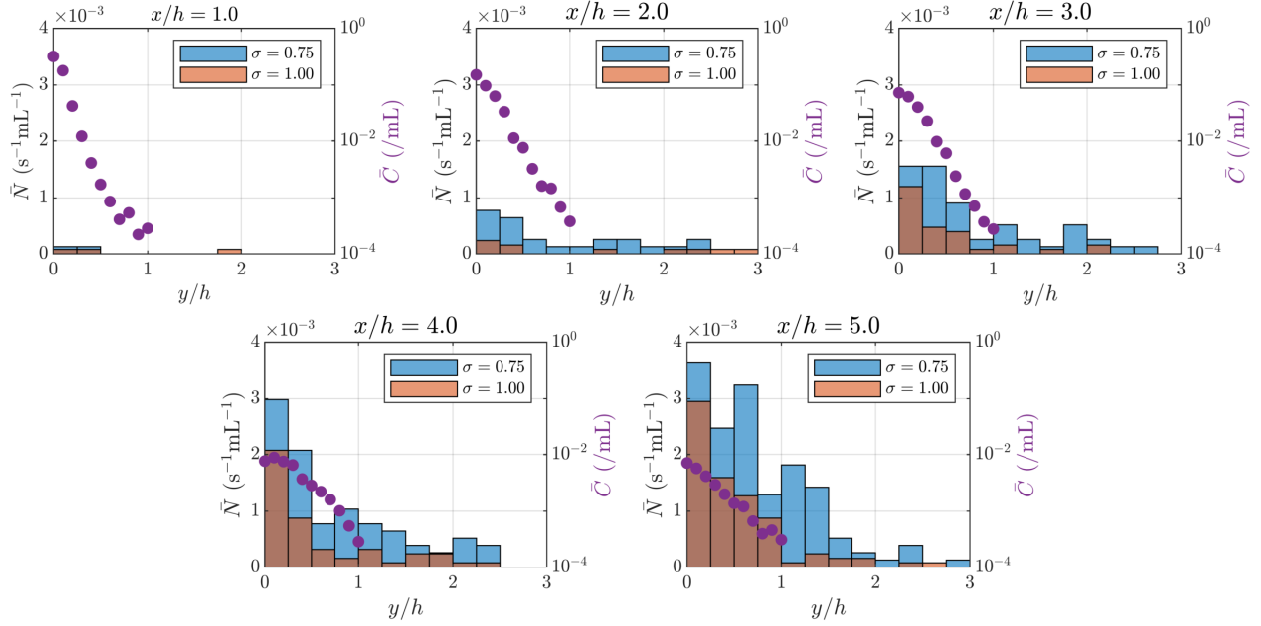


Figure 13: Histograms of the cavitation inception event rate spatial distribution in y direction for $\sigma = 0.75$ and 1 . Histograms are presented for $y - z$ planes located at $x = 1, 2, 3, 4$ and $5h$. Each value represents the sum of all events in the z direction and $0.25h$ each side of the nominal position of the plane in streamwise direction. Additionally, distribution of nuclei concentration from the MSI measurements, averaged in z direction, is shown for each plane. Note the logarithmic scale of the concentration axis.

is observed following an increase in the f_b up to $f_b \approx 13$ kHz. Above that value, the rate of increase reduces due to bubble coalescence in the region downstream of the injection port, as observed via shadowgraphy imaging.

The linear dependence of cavitation event rate on f_b indicates that at these higher σ values, the injected nuclei population is the only active population, and no natural nuclei are being activated. Furthermore, it is important to note that when the bubble injection is stopped, after a short period (order of a few seconds) required for depletion of the BFS re-circulation zone, cavitation completely disappears.

Scatter plots of the locations of incipient events in the $x - z$ and $x - y$ planes obtained from high-speed imaging are presented in figures 10 and 11, respectively, for $\sigma = 0.75$ and 1 . The scatter plots were populated using an algorithm based on examining the difference in the average pixel intensity of the consecutive frames from high-speed imaging from both cameras. If the difference between the pixel intensity of two frames exceeded a threshold value, the location of the pixel with the highest intensity variation in the succeeding frame was recorded as the location of an incipient event. Overall, 681 and 492 events were detected in 61.7 s and 100.3 s of captured data, for $\sigma = 0.75$ and 1 , respectively.

Distribution of the incipient events in $x - z$

plane assumes the topology characteristic of the BFS shear layer, with a peak density in the region about $4 - 5h$ downstream of the step and $0.5 - 1h$ below the tunnel ceiling. Occasional outlying points at the vertical positions between $1.5h \leq z \leq 2$ were manually confirmed as cavitation events and are most likely attributable to the expulsion of vortical structures from the shear layer deeper into the freestream flow. The presented distributions are similar to those reported by Agarwal *et al.* (2018) and Barbaca *et al.* (2020) for the flow with a natural nuclei population.

Distribution of the incipient events in $x - y$ plane has a region of maximum density coinciding with the boundaries of dispersion of the injected nuclei plume. However, a considerable number of events was detected outside of the plume region. This can be attributed to a gradual dispersion in the y direction of the injected bubbles and/or the bubbly products generated by cavitation that get captured within the step large re-circulation zone. While the MSI measurements indicate that bubbles remain within the plume, due to the time-scales involved with the data acquisition, three dimensionality of the flow stemming from a step model with a moderate aspect ratio (≈ 6) and large volume of re-circulation region, a very low concentration bubble population appears to disperse across the whole

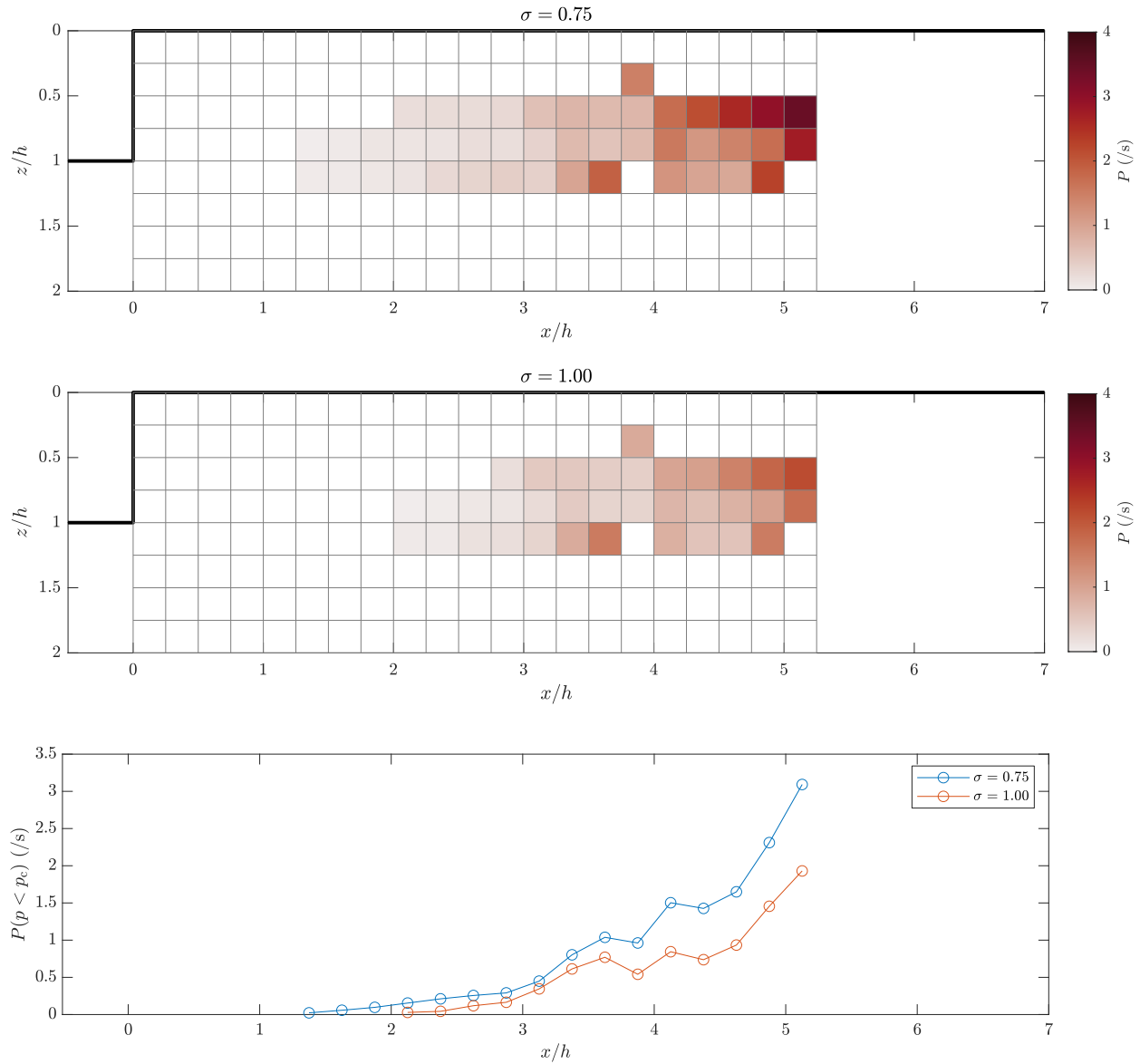


Figure 14: Mapping of the spatial distribution of the cavitation susceptibility in the BFS shear layer in $x-z$ plane for $\sigma = 0.75$ and 1. Cavitation susceptibility is obtained by dividing the cavitation inception event rate with the nuclei concentration for each discretization point ($0.25 \times 0.25 \times 0.25h$ cell) and then averaging the value across the tunnel span. The bottom plot represents the x distribution of the sum of the averaged cavitation susceptibility in the z direction.

span of the step wake. While the bubble concentration outside of the plume is very low, it results with a notable number of cavitation events as the number of bubbles contained in this large volume is significant. The ratio of in and out of plume events appears to be consistent between the two σ values examined, suggesting that the phenomena is not related to activation of the natural nuclei, i.e. no relative increase in the number of out of plume events was observed at the lower σ value. While the characterization of out of plume bubble population is within the capabilities of the MSI method used, due to extremely long time period required to acquire a statistically converged result, it was considered impracticable for this experimental campaign.

In order to reconcile the volumetrically continuous measurements of cavitation inception distribution and the discrete nuclei spatial distribution measurements, results have to be converted into mutually compatible discretized datasets. To do so, both datasets are discretized into cells $0.25h \times 0.25h \times 0.25h$ in x , y and z directions. A sample dataset generated using this process is presented in figure 12. Mapping of spatial distribution of cavitation inception rate in the BFS shear layer for $\sigma = 0.75$ and 1 is shown discretized into $0.25 \times 0.25h$ cells in $x-z$ plane and for a $0.25h$ cell at the tunnel mid-span in y direction. A second order Savitzky-Golay digital filter is used to obtain a better estimate of the distribution from the sparse raw data. The discretized data shows a smooth distribution of cavitation events across the $x-z$ centre plane, with an approximately twofold increase in the number of events between the two σ values distributed uniformly across the cells. Additionally, the spatial distribution of the nuclei content discretized using the same grid is shown in the bottom of the image. A clear outline of the injected nuclei plume is observable in the discretized data.

Discretized cavitation inception data is presented in figure 13 as histograms of event rate spatial distribution in y direction for $\sigma = 0.75$ and 1. The histograms are presented for five spanwise planes located $x = 1, 2, 3, 4$ and $5h$ downstream of the step. Each $0.25h$ wide histogram box is obtained as the sum of all events in the vertical direction and $0.25h$ each side of the nominal x position of the plane. Additionally, the nuclei content distribution from the MSI measurements, averaged in the z direction, is shown for each plane. Note that the concentration axis of the MSI measurements has a logarithmic scale.

The histograms synthesize the observations from the scatter plots, showing the high density of the cavitation events within the plume boundaries and a considerable number of events outside of the plume. A twofold increase in the number of events between the two investigated σ values nominally uniformly

distributed across the span can also be observed. While the maximum nuclei concentration reduces about two orders of magnitude between the most upstream and the most downstream plane, the number of cavitation events between these planes increases by approximately an order of magnitude, indicating a large increase in the cavitation susceptibility.

Discretized values of cavitation susceptibility can be calculated by dividing the discretized fields of cavitation inception event rates and nuclei concentrations. Sample mapping of the spatial distribution of cavitation susceptibility in the BFS shear layer in $x-z$ plane for $\sigma = 0.75$ and 1 is presented in figure 14. Data is obtained by dividing the cavitation inception event rate with the nuclei concentration for each discretization point ($0.25 \times 0.25 \times 0.25h$ cell) and then averaging the value across the y direction. Averaging in the y direction may be performed as the flow is nominally two dimensional and therefore the ensemble average of the cavitation susceptibility (unsteady pressure field) should be representative of any plane across the span. To avoid division by zero for the cells where nuclei concentration is either zero or not measured, but inception events are observed, these are removed from the dataset.

Spatial distributions of cavitation susceptibility indicate the region of highest susceptibility about $5h$ downstream of the step and $0.75h$ below the tunnel ceiling. These distributions compare favourably with the mapping of cavitation susceptibility obtained experimentally by Agarwal *et al.* (2018) and numerically by Brandao & Mahesh (2022) for a step model one tenth of the scale.

The bottom plot in figure 14 represents the streamwise distribution of the averaged cavitation susceptibility summed in z direction for $\sigma = 0.75$ and 1. As expected, a decrease in σ results with an increase in the cavitation susceptibility across all the streamwise locations, while also extending the region susceptible to cavitation further upstream towards the step.

CONCLUSIONS

Characterization of the effects of nucleation on cavitation inception in a high Reynolds number shear layer in the wake of a BFS has been performed using a controlled nuclei population. This was achieved via targeted seeding of the flow with near monodisperse nuclei sufficiently larger than those contained within the water natural nuclei content. Additionally, the spatial distribution of the nuclei was statistically characterized using a volumetric nuclei measurement technique based on MSI.

Targeted seeding through the surface of the BFS model proved to be challenging. Due to bubble break-up associated with high velocity gradient and

shear between the injection and free-stream flows, the generation method routinely used at CRL was found to be unsuitable in this case. A novel method based on inertial pinch-off of air bubbles via high shear at the injection port has been developed to overcome this issue.

Seeding the flow with large nuclei largely addressed the issue of secondary re-nucleation of the BFS re-circulation zone by the products of the incipient cavitation events previously observed for the same flow with a natural nuclei population. However, detection of incipient events outside of the bubbly plume boundaries indicates that injected bubbles and/or cavitation products are still captured by the re-circulating flow and dispersed across the tunnel span. Three-dimensionality of the flow stemming from a moderate step aspect ratio and the existence of a large re-circulation volume make the absolute control of the local nuclei content extremely challenging and therefore the use of a different model geometry would be beneficial. A geometry more suitable for nucleation experiment would need to be highly two-dimensional without the tendency to capture and store nuclei in regions of re-circulating flow.

While some of the issues still remain unresolved, mapping of the spatial distribution of cavitation susceptibility, obtained by combining the cavitation inception and nuclei concentration maps, compares favourably with those reported for the same geometry in the literature. Therefore, current work provides a detailed dataset which is particularly valuable for development of computational tools used for modelling of cavitation inception in nucleated flows.

ACKNOWLEDGEMENTS

The authors wish to acknowledge the assistance of Mr Robert Wrigley and Mr Steven Kent in carrying out the experiments. The authors wish to acknowledge the support of Australian Defence Science and Technology Group within the framework of the University of Tasmania collaborative work on Office of Naval Research 2017 US Multidisciplinary University Research Initiative (MURI) entitled "Predicting turbulent multi-phase flows with high-fidelity: a physics-based approach".

REFERENCES

- Agarwal, K., Ram, O. & Katz, J. 2018 Cavitating structures at inception in turbulent shear flow. In *Proceedings of the 10th International Symposium on Cavitation*.
- Agarwal, K., Ram, O., Wang, J., Lu, Y. & Katz, J. 2020 Measuring the 3D pressure field and relating it to cavitation inception in a turbulent shear layer. In *Proceedings of the 33rd Symposium on Naval Hydrodynamics*.
- Agarwal, K., Ram, O., Wang, J., Lu, Y. & Katz, J. 2021a Reconstructing velocity and pressure from noisy sparse particle tracks using constrained cost minimization. *Experiments in Fluids* **62** (4), 75.
- Agarwal, K., Ram, O., Wang, J., Lu, Y. & Katz, J. 2021b Reynolds number effects on pressure fluctuations and cavitation inception in a turbulent shear layer. In *Proceedings of the 11th International Symposium on Cavitation*.
- Barbaca, L., Paul, R. A., Pearce, B. W. & Brandner, P. A. 2021 Microbubble production in a confined cavitating radial jet. In *Proceedings of the 11th International Symposium on Cavitation*.
- Barbaca, L., Venning, J. A., Russell, P. S., Russell, E. S. C., Pearce, B. W. & Brandner, P. A. 2020 Dynamics of cavitation inception in high Reynolds number shear flow. In *Proceedings of the 33rd Symposium on Naval Hydrodynamics*.
- Belle, A., Brandner, P. A., Pearce, B. W., de Graaf, K. L. & Clarke, D. B. 2016 Artificial thickening and thinning of cavitation tunnel boundary layers. *Experimental Thermal and Fluid Science* **78**, 75–89.
- Bernal, L. P. & Roshko, A. 1986 Streamwise vortex structure in plane mixing layers. *Journal of Fluid Mechanics* **170**, 499–525.
- Brandao, F. L., Madabhushi, A., Bhatt, M. & Mahesh, K. 2020 Large eddy simulation for the investigation of different regimes of cavitation. In *Proceedings of the 33rd Symposium on Naval Hydrodynamics*.
- Brandao, F. L. & Mahesh, K. 2022 Large-eddy simulation of cavitation inception in a shear flow. *International Journal of Multiphase Flow* **146**, 103865.
- Brandner, P.A., Lecoffre, Y. & Walker, G.J. 2006 Development of an Australian national facility for cavitation research. In *Sixth International Symposium on Cavitation - CAV 2006*.
- Brandner, P.A., Lecoffre, Y. & Walker, G.J. 2007 Design considerations in the development of a modern cavitation tunnel. In *Proceedings of the 16th Australasian Fluid Mechanics Conference, 16AFMC*, pp. 630–637.
- Doolan, C., Brandner, P., Butler, D., Pearce, B., Moreau, D. & Brooks, L. 2013 Hydroacoustic characterization of the AMC cavitation tunnel. In *Acoustic 2013, Victor Harbour, Australia*.

- Franc, J. P. & Michel, J. M. 2004 *Fundamentals of Cavitation, Fluid Mechanics and Its Applications*, vol. 76. Dordrecht: Kluwer Academic Publishers.
- Iyer, C. O. & Ceccio, S. L. 2002 The influence of developed cavitation on the flow of a turbulent shear layer. *Physics of Fluids* **14** (10), 3414–3431.
- Katz, J. & O’Hern, T. J. 1986 Cavitation in large scale shear flows. *Journal of Fluids Engineering* **108** (3), 373–376.
- Khoo, M. T., Venning, J. A., Pearce, B. W., Takahashi, K., Mori, T. & Brandner, P. A. 2020 Natural nuclei population dynamics in cavitation tunnels. *Experiments in Fluids* **61** (2), 34.
- Lasheras, J. C., Cho, J. S. & Maxworthy, T. 1986 On the origin and evolution of streamwise vortical structures in a plane, free shear layer. *Journal of Fluid Mechanics* **172**, 231–258.
- O’Hern, T. J. 1990 An experimental investigation of turbulent shear flow cavitation. *Journal of Fluid Mechanics* **215**, 365–391.
- Russell, P. S., Barbaca, L., Venning, J. A., Pearce, B. W. & Brandner, P. A. 2020a Measurement of nuclei seeding in hydrodynamic test facilities. *Experiments in Fluids* **61** (3), 79.
- Russell, P. S., Venning, J. A., Pearce, B. W. & Brandner, P. A. 2020b Calibration of mie scattering imaging for microbubble measurement in hydrodynamic test facilities. *Experiments in Fluids* **61** (4), 93.
- Venning, J. A., Khoo, M. T., Pearce, B. W. & Brandner, P. A. 2018 Background nuclei measurements and implications for cavitation inception in hydrodynamic test facilities. *Experiments in Fluids* **59** (4), 71.